Electronic Supplementary Material (ESI) for Journal of Materials Chemistry A.

2D Anti-MXene Borides Monolayers: Unveiling a Promising New Family of Catalysts for the Nitrogen Reduction Reaction

Viet Q.Bui,*[1] Dinh Quang Khieu[2]

[1]Advanced Institute of Science and Technology, The University of Danang, 41 Le Duan, Danang, Vietnam.

[2]University of Sciences, Hue University, 77 Nguyen Hue, Hue city, Vietnam.

*E-mail of corresponding author: bqviet@ac.udn.vn; mrbuiquocviet@gmail.com

Computational Details

Dynamic Stability

The dynamic stability of the anti-MXene borides was evaluated by calculating their phonon dispersion spectra using the density functional perturbation theory (DFPT) as implemented in the Vienna Ab initio Simulation Package (VASP) and the phonopy package. Phonon frequencies were computed throughout the Brillouin zone to ensure no imaginary frequencies ($\sigma_{phonon} > 0\ cm^{-1}$) appeared, indicating dynamic stability.[1] A plane-wave basis set with an energy cutoff of 450 eV was employed, and the exchange-correlation effects were described using the generalized gradient approximation (GGA) with the Perdew-Burke-Ernzerhof (PBE) functional. A k-point grid of 12×12×1 was used for the structural optimizations.

Mechanical Stability

The mechanical stability of the anti-MXene borides was assessed by calculating their elastic constants (C_{ij}) using stress-strain relationships derived from density functional theory (DFT) calculations performed with VASP and analyzed using the VASPKIT tool.[2] The mechanical stability criteria were based on the Born–Huang's criteria for 2D materials, requiring that $C_{11} > 0$, $C_{66} > 0$, and $C_{11}C_{22} - C_{12}^2 > 0$.[3,4] These criteria ensure the structures can sustain mechanical deformations without undergoing instability. Elastic constants were calculated by applying small deformations to the optimized structures and computing the resulting stress tensors. A plane-wave cutoff energy of 450 eV was used, with the PBE functional employed to describe exchange-correlation effects.

Thermal Stability

Thermal stability of the anti-MXene borides was evaluated using ab initio molecular dynamics (AIMD) simulations conducted at 500 K. The simulations were performed for a total duration of 5 ps with a time step of 1 fs. These calculations were carried out using the VASP package.

The systems were equilibrated in the canonical (NVT) ensemble using the Nosé-Hoover thermostat to control the temperature.[5] The stability of the structures was monitored by observing the total energy and temperature fluctuations throughout the simulation period. The absence of significant structural distortions or energy spikes indicated thermal stability at the elevated temperature.

Solvation Effects

To incorporate solvation effects, we employed the Conductor-like Screening Model (COSMO)[6] within the VASPsol framework to simulate the solvent environment.[7] This method approximates the solvent as a polarizable continuum surrounding the solute, modifying the electrostatic potential in the DFT calculations to account for the dielectric properties of the solvent. Specifically, we set the dielectric constant (ε) to 78.4 to represent aqueous conditions relevant for the electrochemical nitrogen reduction reaction (NRR). This model approximates the solvent as a polarizable continuum surrounding the solute, modifying the electrostatic potential in the DFT calculations to account for the dielectric properties of the solvent. The inclusion of solvation effects is crucial for accurately simulating the electrochemical environment, particularly in an acidic medium (pH ~ 0).

Applied Voltages

The influence of applied voltages was considered by calculating the Gibbs free energy changes of the reaction steps at different electrode potentials. The equilibrium potential for the nitrogen reduction reaction (NRR) was set to -0.17 V, and the limiting potential ($U_{limiting}$) was calculated using the formula:

$$U_{limiting} = \frac{-\Delta G_{PDS}}{e}$$

where ΔG_{PDS} is the free energy change of the potential-determining step (PDS). According 619 to the CHE,[8] the theoretical overpotential (η) is then determined by:

$$\eta = U_{equilibrium} - U_{PDS}$$

Where $U_{equilibrium}$ is the equilibrium potential for the NRR, typically around 0.092 V vs. SHE, which is taken from tabulated experimental standard reduction potentials.[9]

Reaction Kinetics

Reaction kinetics were investigated using the Nudged Elastic Band (NEB) method[10] to identify the minimum energy paths and calculate the activation barriers for the reaction intermediates. Specifically, we focused on the kinetic energy transition from *NN to *NNH, as this step is identified as the rate-determining step (RDS) of the nitrogen reduction reaction (NRR) pathway due to its highest Gibbs free energy barrier among the reaction steps. The NEB calculations provide insights into the transition states and the energy barriers that govern the reaction kinetics, which are essential for understanding the efficiency of the catalytic processes. By pinpointing the exact RDS, we can better evaluate and optimize the performance of catalysts, ensuring that the most critical transition state is accurately characterized and its energy barrier minimized for enhanced catalytic activity. Additionally, we examined the kinetics of the proton transfer in the PDS using the Zundel $H_5O_2^+$ ion as the solvated proton donor.[11] This approach provides a more realistic representation of proton transfer in an aqueous environment, thereby enhancing the accuracy of our kinetic analysis.

φ Descriptor

The φ descriptor is a crucial parameter used to predict the electrocatalytic performance of the 2D anti-MXene borides. This descriptor combines the d-electron count (N_d) and the square root of the electronegativity ($\sqrt{E_{TM}}$) of the transition metals, providing a comprehensive measure of their electronic properties. The relationship between the φ descriptor and the limiting potential

(U_L) for NRR activity is established, revealing that higher φ values correlate with increased limiting potentials. This suggests that the φ descriptor effectively captures the electronic interactions crucial for NRR efficiency.

The formulation and validation of the φ descriptor were inspired by the principles outlined in several key studies. Xu et al. (2018)[12] presented a universal design principle for single-atom electrocatalysts, correlating the local structural and chemical environment of the active centers with their catalytic activity. Niu et al. (2020)[13] further demonstrated the significance of electronic properties in single-atom catalysts supported on g-CN for N_2 reduction. The electronic descriptors for the catalytic activity of transition metals have been extensively studied, providing a foundation for understanding the relationship between electronic structure and catalytic performance. Additionally, recent works by Wang et al. (2021)[14] highlighted the importance of electronic descriptors in screening transition-metal single-atom catalysts for nitrogen fixation, providing a theoretical basis for understanding the relationship between electronic properties and catalytic activity.

In this work, the φ descriptor serves as a predictive tool for assessing the catalytic efficiency of new materials. By incorporating this descriptor into the screening process, the study offers a systematic approach to identifying and optimizing high-performance electrocatalysts for NRR. The robustness of the φ descriptor is supported by its alignment with the established principles in the referenced studies, providing a solid theoretical foundation for its application in predicting NRR activity.

The insights gained from this analysis contribute to a broader understanding of the electronic factors governing catalytic activity, ultimately guiding the development of more efficient and effective NRR catalysts. The use of the φ descriptor enhances the ability to design and select promising electrocatalysts, paving the way for advancements in sustainable ammonia synthesis.

Table S1. Lattice parameters a=b, buckling height h, and the nearest metal-metal distance d for various anti-MXenes borides, along with their corresponding structural form (planar or buckled). The lattice parameter denotes the cell dimension in the plane, the buckling height signifies the vertical displacement between boron atoms, and the nearest metal-metal distance is indicative of the compactness within the lattice structure. Dashed lines separate metals from other element groups.

	a=b (Å)	h (Å)	d (Å)	Structure
TiB	4.359	0	2.180	Planar
ZrB	4.220	1.656	2.267	Buckled
HfB	4.496	1.283	2.338	Buckled
VB	4.057	0.857	2.073	Buckled
NbB	4.157	1.181	2.161	Buckled
TaB	4.200	1.507	2.231	Buckled
CrB	4.029	0	2.014	Planar
MoB	4.014	1.614	2.163	Buckled
WB	3.984	1.721	2.170	Buckled
MnB	3.972	0	1.986	Planar
ReB	3.852	1.817	2.129	Buckled
FeB	3.705	1.100	1.934	Buckled
RuB	3.871	1.460	2.069	Buckled
OsB	3.870	1.561	2.086	Buckled
CoB	3.571	1.323	1.904	Buckled
RhB	3.897	1.286	2.052	Buckled
IrB	3.914	1.370	2.074	Buckled
NiB	3.704	1.094	1.931	Buckled
PdB	4.042	1.113	2.096	Buckled
PtB	4.041	1.217	2.110	Buckled
CuB	3.979	0	1.989	Planar
AgB	4.356	0	2.178	Planar
AuB	4.356	0	2.178	Planar

Table S2. Cohesive energies of anti-MXenes borides (CoB, FeB, IrB, MnB, OsB, ZrB) compared with other two-dimensional materials (borophene, silicene, phosphorene). The cohesive energy values, provided in electronvolts (eV), reflect the stability of the crystal lattice, with lower energies indicating stronger binding within the structure of material. References are cited for the cohesive energies of known materials for comparative purposes.

Structures	Cohesive energy (eV)	References
CoB	-5.413	
FeB	-4.969	
IrB	-6.753	
MnB	-4.503	
OsB	-6.721	
ZrB	-5.563	
Borophene	-5.87	Science 350, 1513 (2015)
Silicene	-4.01	Phys. Rev. Lett. 108, 245501 (2012)
Phosphorene	-4.67	Nat. Nanotechnol. 9, 372 (2014)

Table S3. Comparison table for the NRR performance of catalyst in this work with other reported electrocatalysts in acidic medium.

Catalyst	**Limiting potential (V)**	**References**
FeB	-0.32	This work
V_2-Pc	-0.39	*J. Am. Chem. Soc*. 2020, 142, 5709−5721
B-C_3N_4	-0.47	*J. Am. Chem. Soc.* 2018, 140, 14161−14168
Mo-C_2N	-0.53	*Phys. Chem. Chem. Phys.* 2018, 20, 12835−12844
Mo−graphdiyne	-0.99	*J. Am. Chem. Soc.* 2019, 141, 10677−10683
B@ReS_2	-0.53	*Phys. Chem. Chem. Phys.*, 2023,25, 25389-25397
Ru−N_3	-1.1	*Adv. Mater.* 2018, 30, 1803498-1803503
Ru-ZrO_2	-1.41	*Chem.* 2019, 5, 204-214
BN	-0.45	*J. Am. Chem. Soc.* 2019, 141, 2884-2888
B@g-CN	-0.15	*Nano Lett.* 2019, 19, 9, 6391–6399

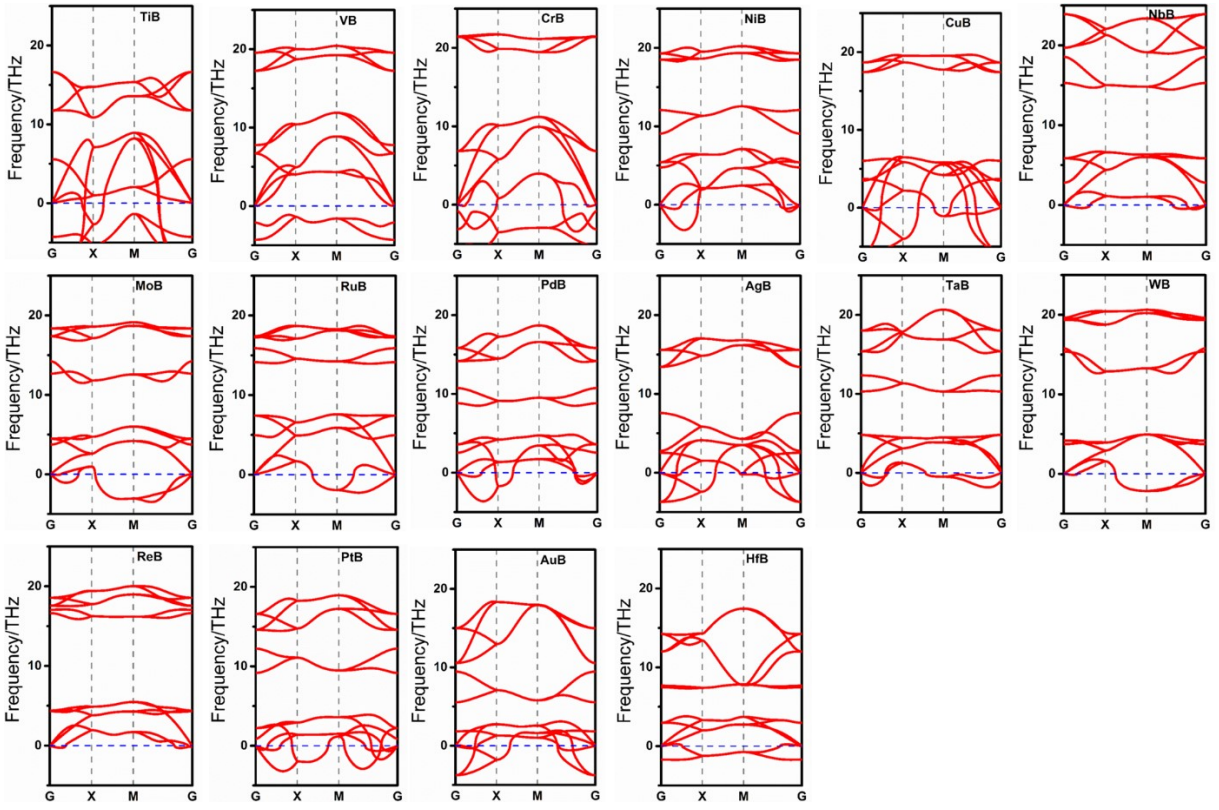

Figure S1. Phonon dispersion curves for sixteen anti-Mxenes borides compounds, displaying the phonon spectra with respective small or large imaginary frequency regions. The curves indicate the vibrational stability of the materials, where imaginary frequencies (depicted as negative values) suggest dynamic instability within the crystal lattice. Each panel corresponds to a different MB compound, with the high symmetry points in the Brillouin zone marked as G (Gamma), X, and M.

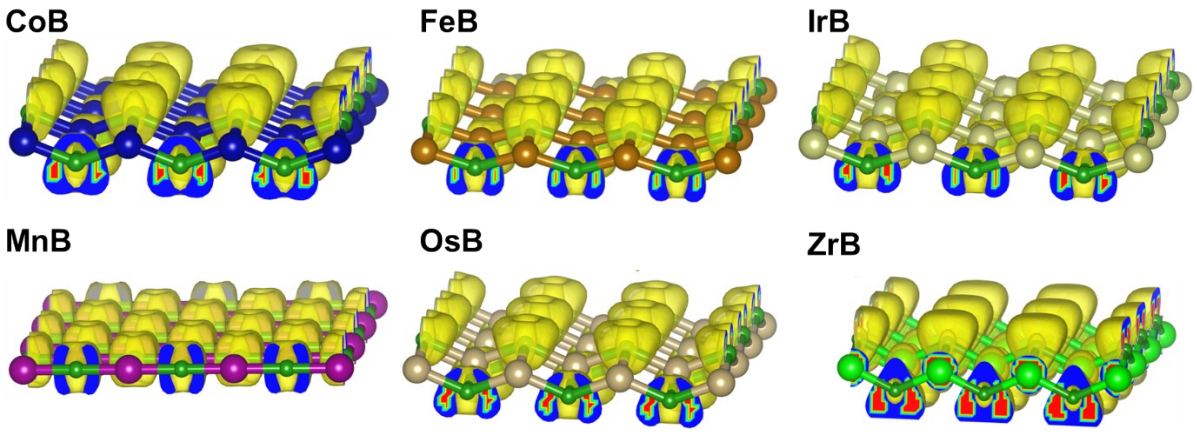

Figure S2. Electron localization function (ELF) plots for six stable anti-MXenes borides: CoB, FeB, IrB, MnB, OsB, and ZrB. The plots illustrate the spatial distribution of electron localization, highlighting areas of high electron density and the nature of chemical bonding within the structures. The ELF isosurface is rendered at a value of $\rho = 0.3$ to visualize regions of significant electron localization.

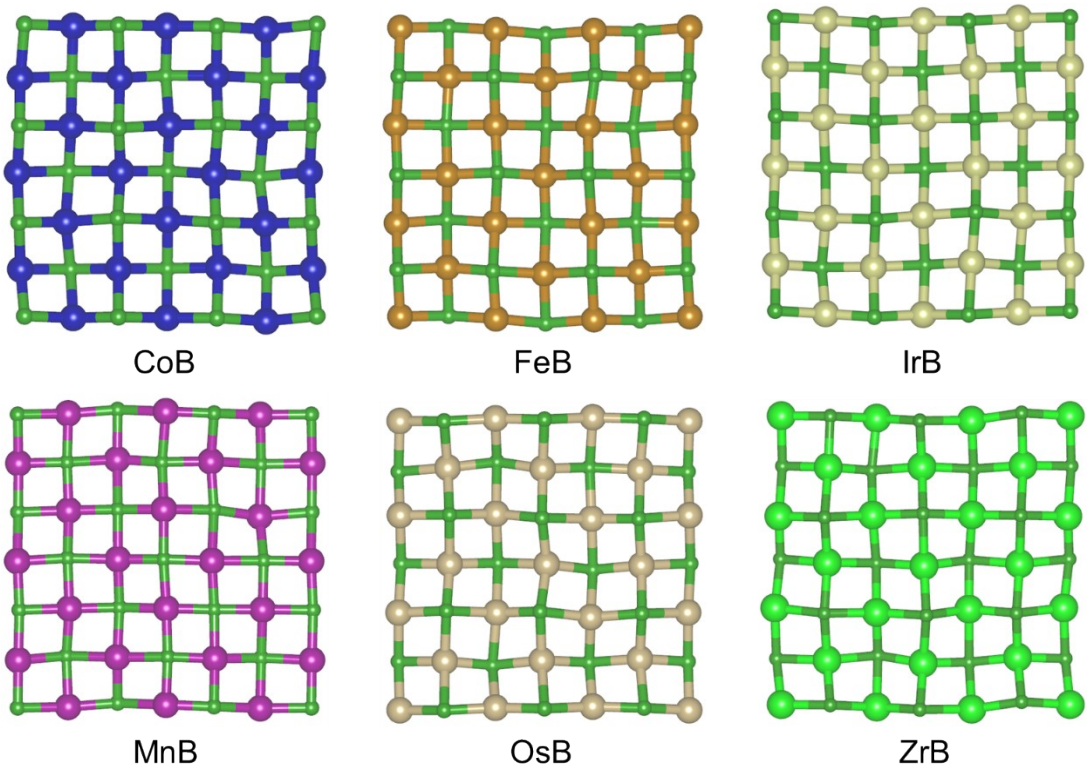

Figure S3. Snapshots of six anti-MXenes borides (CoB, FeB, IrB, MnB, OsB, ZrB) from the final step of 5 ps ab initio molecular dynamics (AIMD) simulations at 500 K. These images illustrate the robustness of the structures, as evidenced by the minimal structural distortion observed over the course of the AIMD simulation period, highlighting their thermal stability at elevated temperatures.

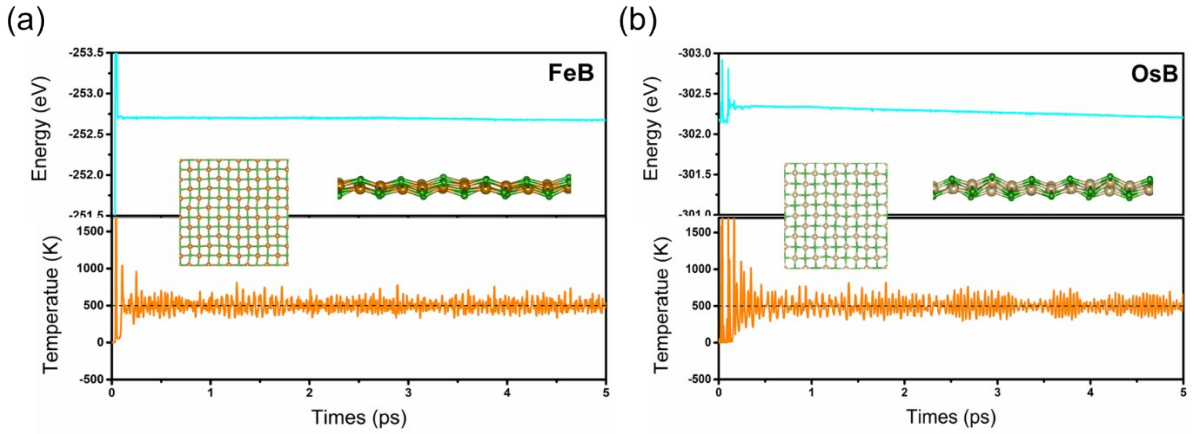

Figure S4. Energy and temperature profiles for FeB (a) and OsB (b) during the final 5 ps of ab initio molecular dynamics (AIMD) simulations at 500 K. Insets show the stable structures of the MB monolayers. The total energy of the system remains consistent throughout the simulation, indicating stability, while the temperature fluctuates around the target temperature, demonstrating the dynamical stability of the monolayers under thermal conditions.

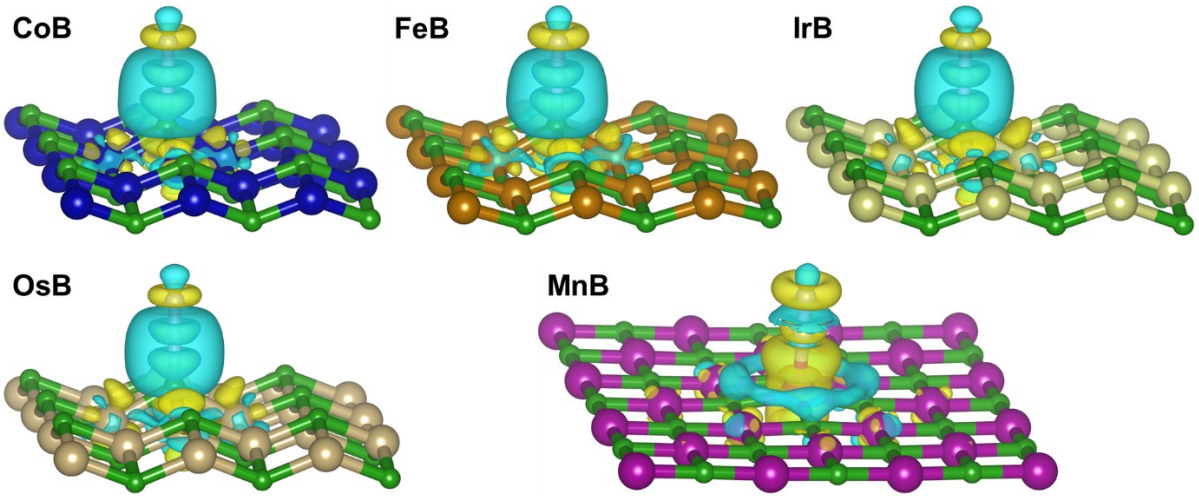

Figure S5. Visualization of charge density differences for five anti-MXenes Borides (CoB, FeB, IrB, MnB, OsB) with an isosurface threshold set at 0.009. Regions of charge accumulation are represented by yellow shading, while areas of charge depletion are shown in blue. These visualizations highlight the electron distribution changes upon adsorption or interaction with other species.

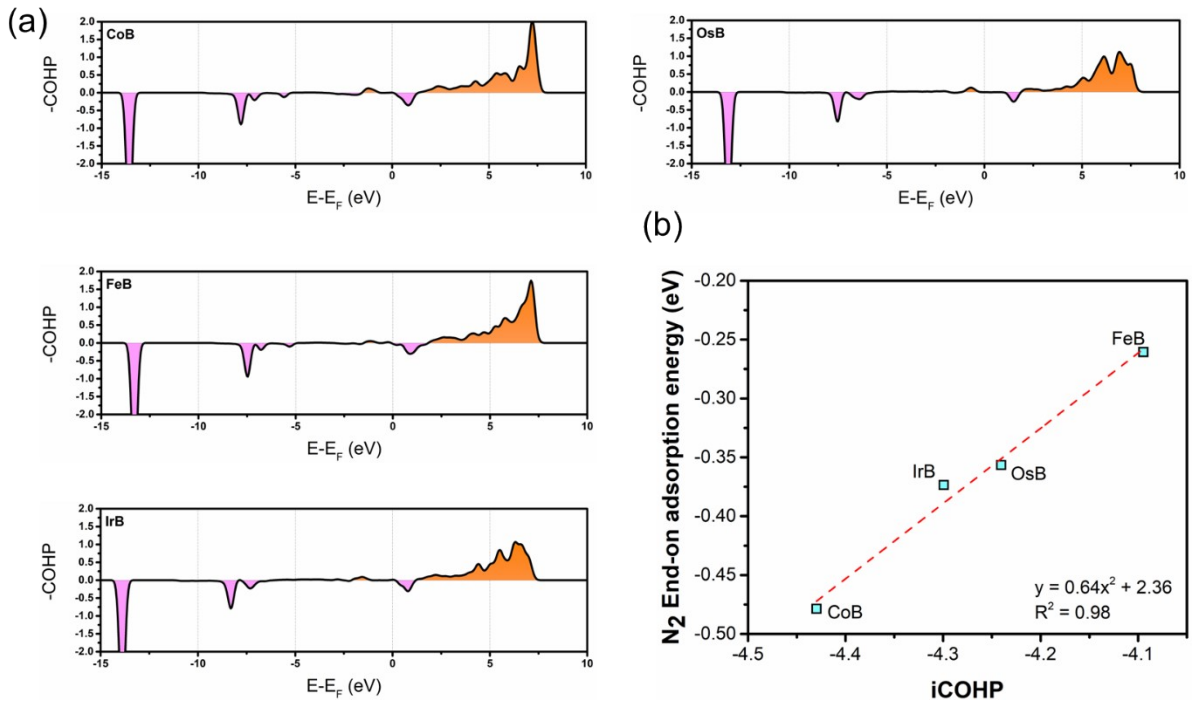

Figure S6. (a) Integrated crystal orbital Hamilton population (ICOHP) for B-N bonding at the active sites in CoB, MnB, FeB, OsB, and IrB. The ICOHP values plotted against the energy levels relative to the Fermi energy ($E-E_F$) show that positive values indicate bonding interactions, while negative values suggest antibonding interactions. The magnitude of ICOHP is indicative of the bond strength, with higher values reflecting stronger bonding or antibonding character; (b) Relationship between iCOHP and N_2 end-on adsorption energy, where more negative iCOHP values correspond to stronger B-N bonding and more favorable N_2 adsorption.

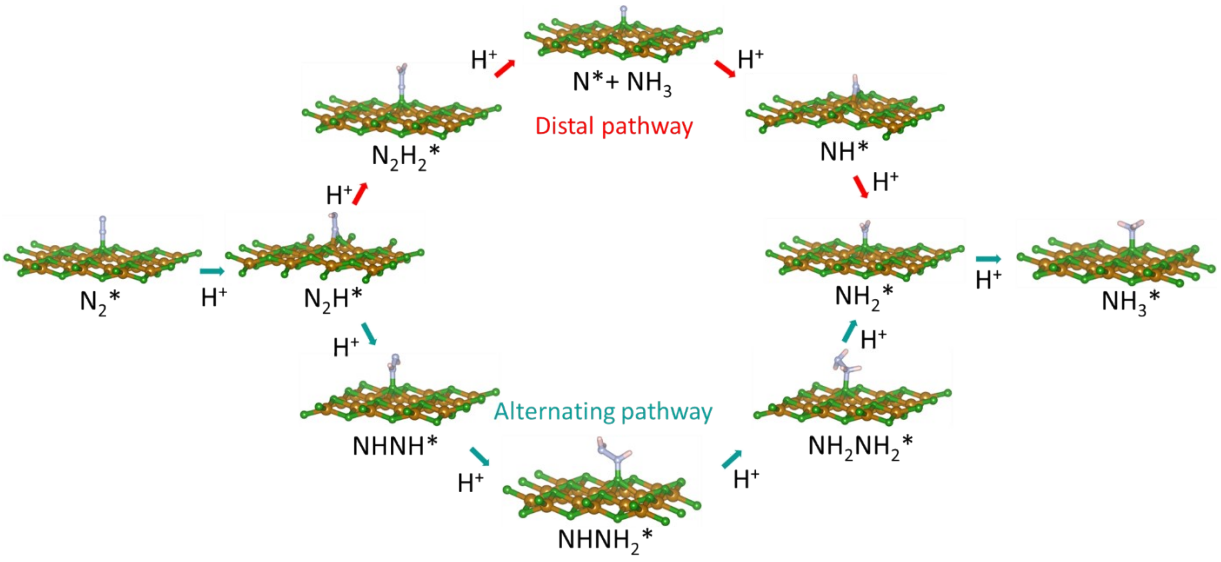

Figure S7. Schematic representation of the NRR pathways on anti-MXene borides surfaces: the distal pathway (top row) and the alternating pathway (bottom row). Each step depicts the progression of N2 reduction, with key intermediates and the direction of electron flow indicated by arrows. The red arrows represent the sequence of steps in the distal pathway, while the blue arrows correspond to the steps in the alternating pathway, culminating in the formation of NH3.

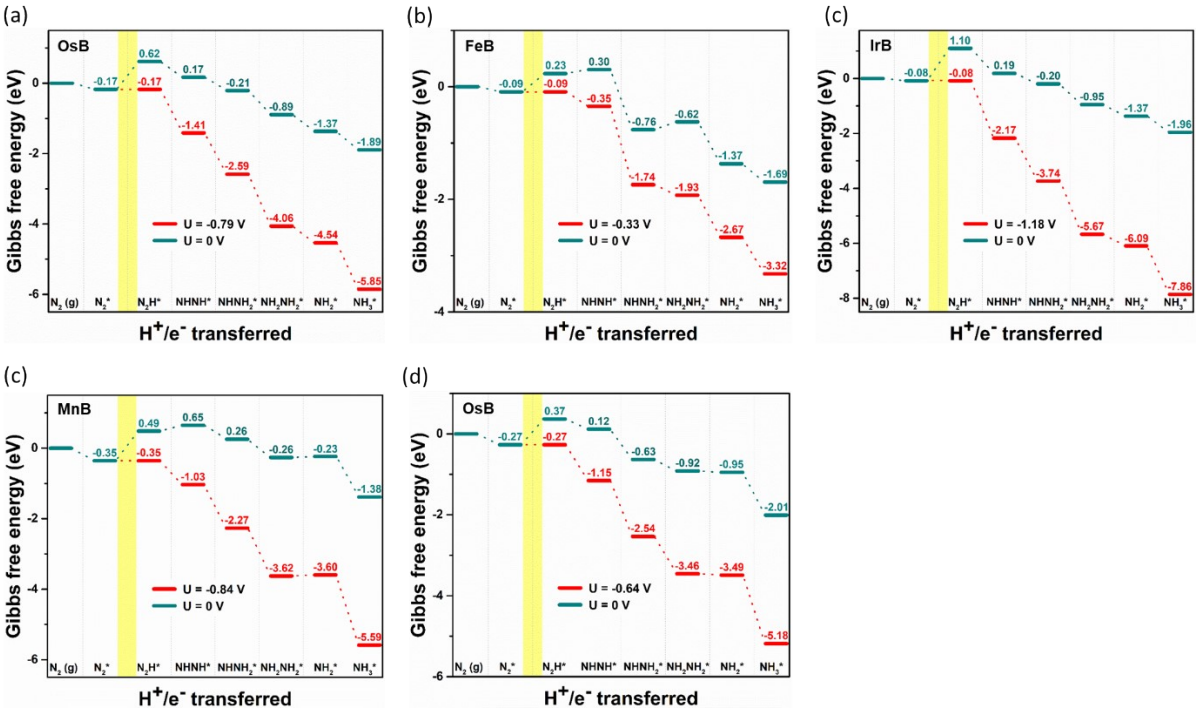

Figure S8. Gibbs free energy diagrams for N_2 to NH_3 electroreduction on (a) CoB, (b) FeB, (c) IrB, (d) MnB, and (e) OsB monolayers, with applied voltages of U = 0 V (solid blue) and U = -0.79 V, -0.33 V, -1.18 V, -0.84 V, -0.64 V (solid red) respectively.

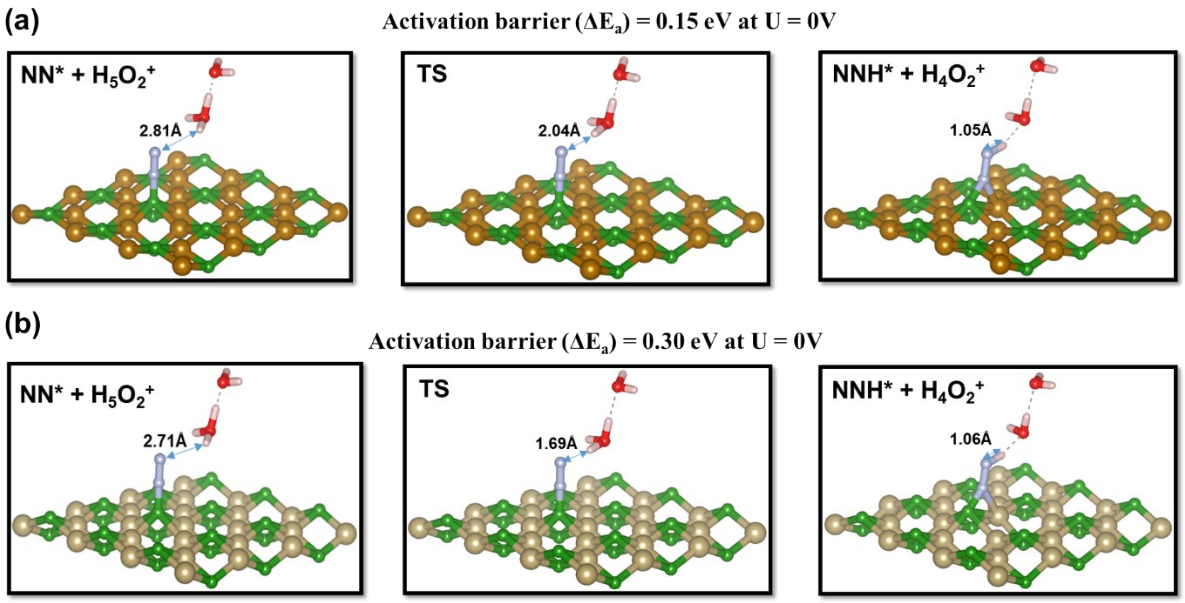

Figure S9. Optimized structures and related kinetic barriers of reduction of NN* to NNH* on (a) FeB and (b) OsB surfaces

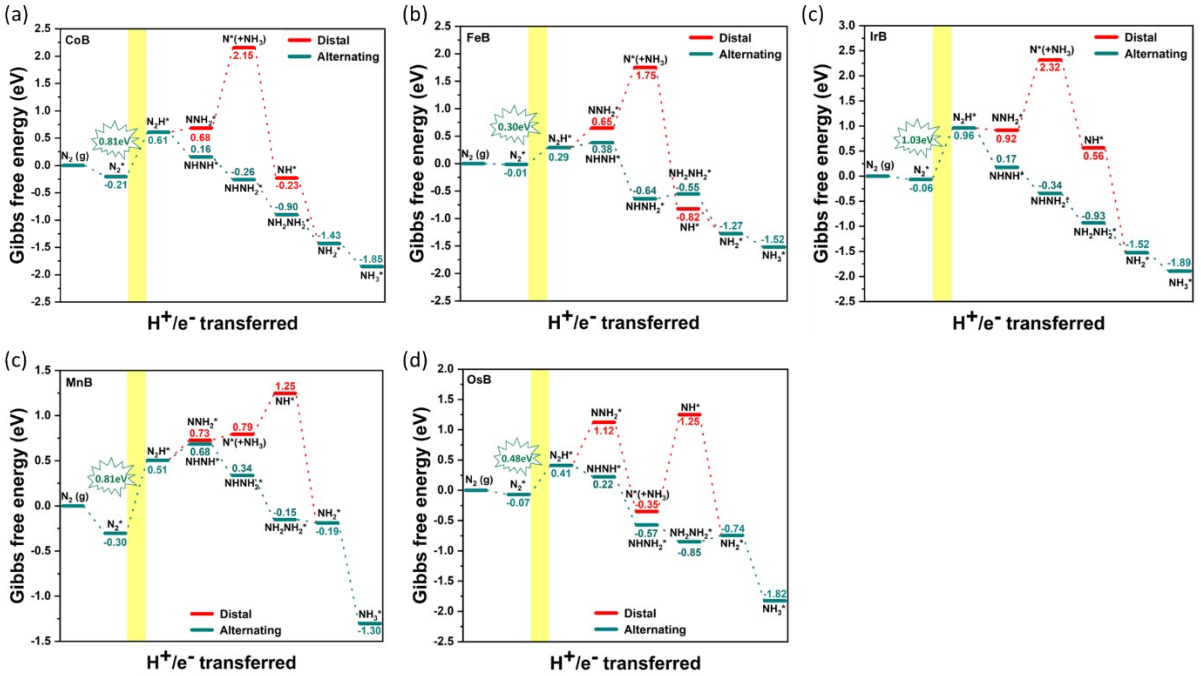

Figure S10. Gibbs free energy diagrams for N_2 to NH_3 electroreduction on (a) CoB, (b) FeB, (c) IrB, (d) MnB, and (e) OsB monolayers, with distal (solid red) and alternating (dashed red) pathways and their energy values. Calculations include solvation effects using VASPsol.

References

1. Togo, A., & Tanaka, I. (2015). First principles phonon calculations in materials science. *Scripta Materialia*, *108*, 1-5.
2. Wang, V., Xu, N., Liu, J. C., Tang, G., & Geng, W. T. (2021). VASPKIT: A user-friendly interface facilitating high-throughput computing and analysis using VASP code. *Computer Physics Communications*, *267*, 108033.
3. Born, M., & Huang, K. (1996). *Dynamical theory of crystal lattices*. Oxford university press.
4. Wang, H., Li, T., Liu, X., Zhu, W., Chen, Z., Li, Z., & Yang, J. *(2023).* mech2d: An Efficient Tool for High-Throughput Calculation of Mechanical Properties for Two-Dimensional Materials. *Molecules, 28*(11), 4337.
5. Nosé, S. (1984). A unified formulation of the constant temperature molecular dynamics methods. *The Journal of chemical physics*, *81*(1), 511-519.
6. Klamt, A., & Schüürmann, G. J. G. J. (1993). COSMO: a new approach to dielectric screening in solvents with explicit expressions for the screening energy and its gradient. *Journal of the Chemical Society, Perkin Transactions 2*, (5), 799-805.
7. Mathew, K., Sundararaman, R., Letchworth-Weaver, K., Arias, T. A., & Hennig, R. G. (2014). Implicit solvation model for density-functional study of nanocrystal surfaces and reaction pathways. *The Journal of chemical physics*, *140*(8).
8. Nørskov, J. K., Rossmeisl, J., Logadottir, A., Lindqvist, L. R. K. J., Kitchin, J. R., Bligaard, T., & Jonsson, H. (2004). Origin of the overpotential for oxygen reduction at a fuel-cell cathode. *The Journal of Physical Chemistry B*, *108*(46), 17886-17892.
9. Lindley, B. M., Appel, A. M., Krogh-Jespersen, K., Mayer, J. M., & Miller, A. J. (2016). Evaluating the thermodynamics of electrocatalytic N2 reduction in acetonitrile. *ACS Energy Letters*, *1*(4), 698-704.
10. Henkelman, G., Uberuaga, B. P., & Jónsson, H. (2000). A climbing image nudged elastic band method for finding saddle points and minimum energy paths. *The Journal of chemical physics*, *113*(22), 9901-9904.
11. Dahms, F., Costard, R., Pines, E., Fingerhut, B. P., Nibbering, E. T., & Elsaesser, T. (2016). The hydrated excess proton in the Zundel cation H5O2+: The role of ultrafast solvent fluctuations. *Angewandte Chemie International Edition*, *55*(36), 10600-10605.
12. Xu, H., Cheng, D., Cao, D., & Zeng, X. C. (2018). A universal principle for a rational design of single-atom electrocatalysts. *Nature Catalysis, 1*(5), 339-348.
13. Niu, H., Wang, X., Shao, C., Zhang, Z., & Guo, Y. (2020). Computational screening single-atom catalysts supported on g-CN for N2 reduction: high activity and selectivity. *ACS Sustainable Chemistry & Engineering, 8*(36), 13749-13758.
14. Wang, J., Zhang, Z., Li, Y., Qu, Y., Li, Y., Li, W., & Zhao, M. (2021). Screening of transition-metal single-atom catalysts anchored on covalent–organic frameworks for efficient nitrogen fixation. *ACS Applied Materials & Interfaces, 14*(1), 1024-1033.